Martín-Asensio *et al.*
Micro and Nano Systems Letters (2024) 12:22
https://doi.org/10.1186/s40486-024-00213-1

Micro and Nano Systems Letters

CORRESPONDENCE

Open Access

Investigating non fluorescence nanoparticle transport in Matrigel-filled microfluidic devices using synchrotron X-ray scattering

Alberto Martín-Asensio[1], Irene Pardo[1], Rocío Mesa[1], Demian Pardo[1], Juan P. Fernández-Blázquez[2], Juan Carlos Martínez-Guil[3], Milagros Castellanos[1], Jaime J. Hernández[1*], Álvaro Somoza[1] and Isabel Rodríguez[1]

Abstract

The present study explores the application of X-ray scattering, using synchrotron radiation, to assess the diffusive transport of nanomedicines in tumor on a chip devices fabricated by 3D stereolithography using a resin with high optical and X-ray transmittance. Unlike conventional methods that require fluorescent labeling of nanoparticles, potentially altering their in vitro and in vivo behavior, this approach enables the investigation of the transport properties for unlabeled nanoparticles. In particular, the results presented confirm the influence of the porosity of the extracellular matrix-like microenvironment, specifically Matrigel, on the diffusive transport of oligonucleotide-functionalized gold nanoparticles. The analysis of the scattering patterns allows to create 2D maps showing the nanoparticle distribution with high spatial resolution. The proposed approach demonstrates the potential for studying other factors involved in nanoparticle diffusion processes. By implementing X-ray scattering to track unmodified nanomedicines within extracellular matrix-like microenvironments, increasingly accurate models for evaluating and predicting therapeutics transport behaviors can be developed.

Keywords Nanoparticle diffusion, SAXS, Nanomedicines, Tumour-on-a-chip

Introduction

Cancer has become one of the leading causes of death with 19.3 million cases worldwide in 2020 and is predicted to almost double by 2040 [1]. In the past decades, many innovative therapies, such as immunotherapy or molecular-targeted therapy, have shown promise in improving treatment outcomes and reducing side effects [2–4]. It can be anticipated that nanoparticles (NPs) will play a fundamental role in cancer theragnostics due to their unique properties and versatility as carriers. NPs can be engineered to carry therapeutic molecules to cancer cells, and at the same time, they can be designed to incorporate imaging probes and target moieties, allowing for real-time monitoring and precise tumour targeting of the tumour response. Such nanocarriers maximize treatment efficacy while minimizing damage to healthy tissues [5–8]. However, current nanomedicines evaluated in a clinical setting usually present poor efficacy and little accumulation in solid tumours [9–11]. Hence, there is a quest for more accurate pre-clinical models with better predictive power to assess the bioavailability and, ultimately, the efficacy of nanomedicines.

To this end, microfluidic Tumor-on-a-Chip (ToC) devices offer a more accurate preclinical model for nanomedicine evaluation, mimicking the complex tumor microenvironment (TME) better than traditional 2D cell cultures or animal models [12–16]. They provide a dynamic environment and allow the study of

*Correspondence:
Jaime J. Hernández
jaime.hernandez@imdea.org
[1] Madrid Institute for Advanced Studies in Nanoscience (IMDEA Nanociencia), 28049 Madrid, Spain
[2] IMDEA Materials Institute, 28906 Getafe, Madrid, Spain
[3] ALBA Synchrotron Light Source, Cerdanyola del Vallès, 08290 Barcelona, Spain

nanomedicine transport processes through the TME, such as extravasation and penetration of nanomedicines into solid tumour [17–20]. So far, most (if not all) of these studies have been performed using fluorescent NPs [21–23], as they allow us to visualize and track various transport processes within the microfluidic system. Nanomedicines primarily comprise organic nanomaterials such as liposomes, micelles, dendrimers, and polymers as well as metallic-based nanoparticles such as gold or iron-based ones [5, 9, 24, 25]. Labelling these particles with fluorescent markers may alter their diffusion properties, leading to deviations from their behaviour at the in vivo and in vitro conditions. Thus, additional approaches, compatible with ToC devices, are needed to comprehensively study the transport processes of actual unmodified nanomedicines within the recreated TME.

A promising alternative is the use of synchrotron light. X-ray scattering techniques, such as Small and Wide Angle X-ray Scattering (SAXS-WAXS), provide valuable information into NP size, shape, aggregation, crystallinity, or composition [26–30]. In particular, SAXS is a versatile and robust technique that can provide direct and rapid structural information, across nanoscale to mesoscale. It can be applied to a broad range of materials, including polymers, biological molecules, or inorganic nanoparticles studied under different environments (solution, vacuum, variable pressure, flow or temperature, etc.). Furthermore, SAXS does not require crystalline samples, since it relies on the electronic density contrast between the nanoparticle and the background environment and, importantly, it can be easily integrated with microfluidic devices. This technique's capabilities were successfully showcased, for instance, by Coral et al., who employed SAXS to determine the disposition of nanoparticles inside endosomes of the cell cytoplasm [29]. Similarly, Le Goas et al. evaluated the diffusion of nanoparticles through Matrigel-filled borosilicate glass capillaries [31]. The well established integration of scattering techniques with microfluidics enables dynamic studies of nanoparticles under flow conditions, leveraging the high brilliance and penetrating power of synchrotron radiation and providing high spatial and time resolution. In brief, synchrotron radiation is emitted when charged particles, such as electrons, are accelerated to nearly the speed of light and forced to travel in curved paths by magnetic fields. Synchrotron radiation covers a broad wavelengths range and is characterized by its high intensity, orders of magnitude higher than conventional *in-house* X-ray sources. To date, the use of synchrotron radiation in microfluidic environments has been used primarily for real-time in situ synthesis and characterization of NPs [32–34]. In the present work, we demonstrate how X-ray scattering and absorption measurements, using synchrotron radiation, can be exploited to study the diffusion of non-fluorescent NPs in microfluidic devices in real-time. The results presented here pave a promising path for future research endeavours. By leveraging the unique synchrotron light capabilities with the design flexibility of ToC models, valuable new insights into the dynamics and biodynamics [35] of non-fluorescent NP-based therapeutics can be revealed, ultimately serving to improve future nanomedicines.

Results and discussion

The microfluidic devices employed in this work were fabricated using a 3D stereolithographic printer (Asiga MAX X27 UV). The device was designed to have two channels embedded within the 3D printing resin (Fig. 1a). The channels design had a nominal height of 1 mm and a width of 750 µm and were separated by a 200 µm wall (cf. SEM image Fig. 1a). The channel´s size was selected with the consideration that measurements would be performed with a beam size of *ca*. 100 microns. Based on this, the channel size was designed to be large enough so that the beam size would allow for 2D mapping, avoiding X-ray overexposure. The channel aperture size increases from 200 µm on the NPs side to 800 µm on the hydrogel side (cf. Fig. 1a). The connection between the channels was designed with a trapezoidal shape to ensure that the extracellular matrix employed (Matrigel), when filled, is effectively pinned to the channel and prevents it from spreading out into the NPs channel [36]. Two reservoirs were included in the Matrigel channel to introduce the fluids, and two connectors were designed in the NPs channel to connect microfluidic tubing. The chip was fabricated using a biocompatible optical transparent resin (*3D-printing proc3dure GR10*). A picture of the microfluidic device can be seen in Fig. 1b, where a blue colorant has been filled to better visualize the NP channel and let it diffuse into the Matrigel-filled channel. A 2×2 mm^2 thin observation window (400 µm thick) was implemented to further minimize the X-ray absorption. In terms of X-ray transparency, the resin employed is equivalent to that of thermoplastic polymers such as polycarbonate or polystyrene, and far superior to other materials employed in microfluidics, such as PDMS or glass derivatives. Furthermore, it provides the benefits inherent to 3D printing such as excellent design flexibility and fast fabrication.

The X-ray transmittance of the different materials was initially assessed by measuring 1.5 mm thick films using a laboratory X-ray source (SAXSpoint 5.0, Anton-Paar, $\lambda = 1.54$ Å). Figure 1c shows the transmittance values obtained, including, for comparison, those obtained using synchrotron light ($\lambda = 0.99$ Å). In addition, The X-ray transmittance of the 3D resin was evaluated in a 400 µm thick film, equivalent to the chip windows total

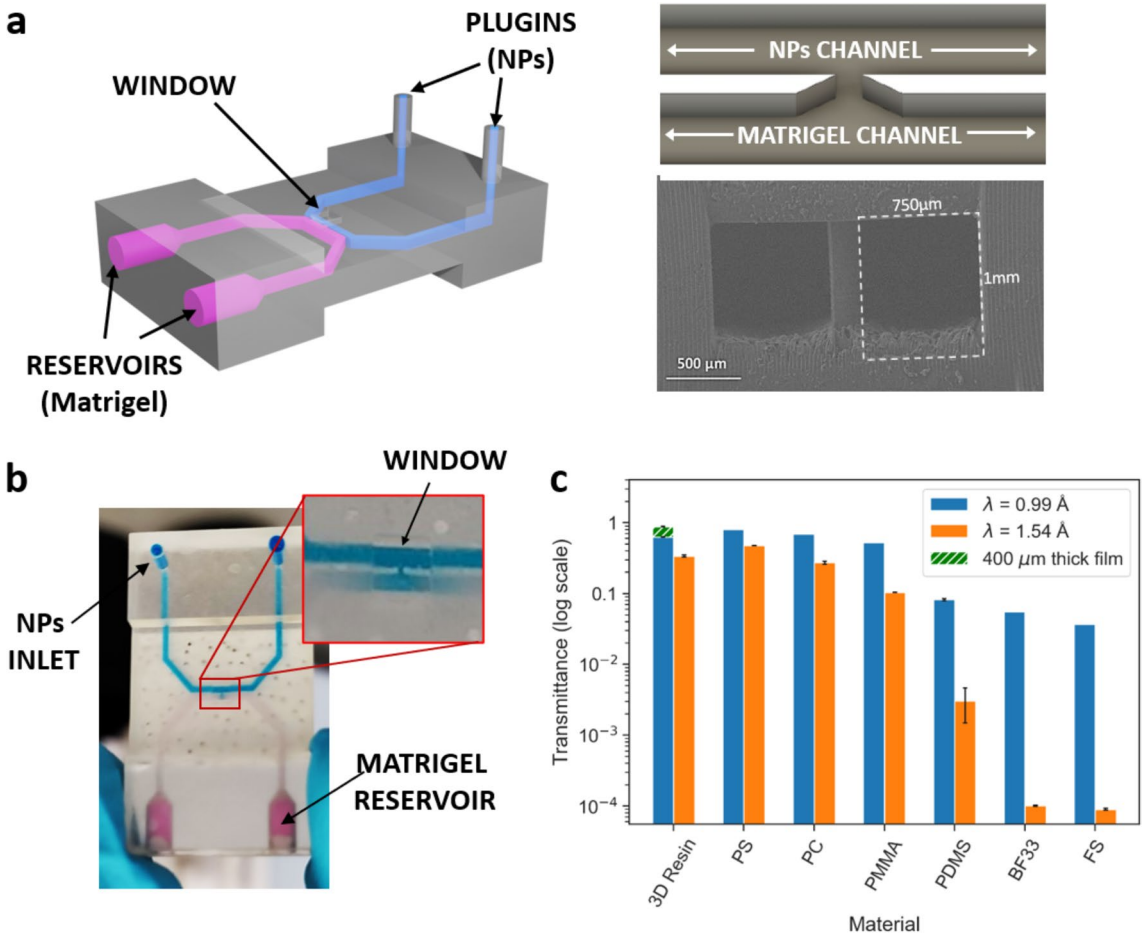

Fig. 1 **a** General view of the digital 3D design (left) and details of the microchannel's region of interest for diffusion measurements and SEM image of the chip cross-section (right). The dashed rectangle indicates the nominal channel dimensions. A residual layer of resin can be observed at the bottom of the channel. **b** Operating 3D printed device with blue colorant diffusing through Matrigel (pink). Matrigel reservoirs and plugins outlets are indicated. **c** X-ray transmittance values were obtained from different materials (1.5 mm thick) at two different wavelengths. Notice that the vertical axis is presented in logarithmic scale. The X-ray transmittance of the 3D resin measured using a λ = 0.99 Å was also evaluated in a 400 µm thick film, equivalent to the chip windows thickness

thickness. Notice that the y-axis is represented in logarithmic scale. These results confirm that the microfluidic device fulfils the main requirements in terms of optical and X-ray transparency and, at the same time, is cost-effective and easily fabricated [37].

In terms of the nanomedicines employed for the study, we selected gold NPs densely functionalized with oligonucleotides, which are known as Spherical Nucleic Acids (SNAs) and present interesting properties for the development of nanomedicines [38–40] and diagnostic tools [41, 42]. Particularly, Au-based SNAs are easy to prepare, non-toxic, very stable, and internalize easily in a wide variety of cell types. For this work, Au NPs were chemically functionalized using an oligonucleotide containing a thiol derivative at the 3'-end. The model sequence selected for this study was a 22 nt-long polythymidine (PolyT), which can be used to obtain very stable SNAs. Gold NPs were synthesized by the Turkevich method [43]. Briefly, a solution of hydrogen tetrachloroaurate (III) hydrate (FisherScientific) 0.23 mM in RNAse-free water was stirred and heated to reflux. Then, a solution of sodium citrate tribasic dehydrate 3.62 mM of citrate, dissolved in the same water, was added, and the mixture was stirred for 15 min. After that time, the solution was allowed to cool down at room temperature, and the Au NPs obtained were filtered through a 20–40 µm glass filter plate with the help of a vacuum pump to get rid of large aggregates, followed by a second filtration with a PES syringe filter of 0.22 µM (Millipore).

Diffusion measurements were performed at the NCD-SWEET BL11 Beamline at the ALBA synchrotron. Figure 2a shows the easy-to-implement experimental setup.

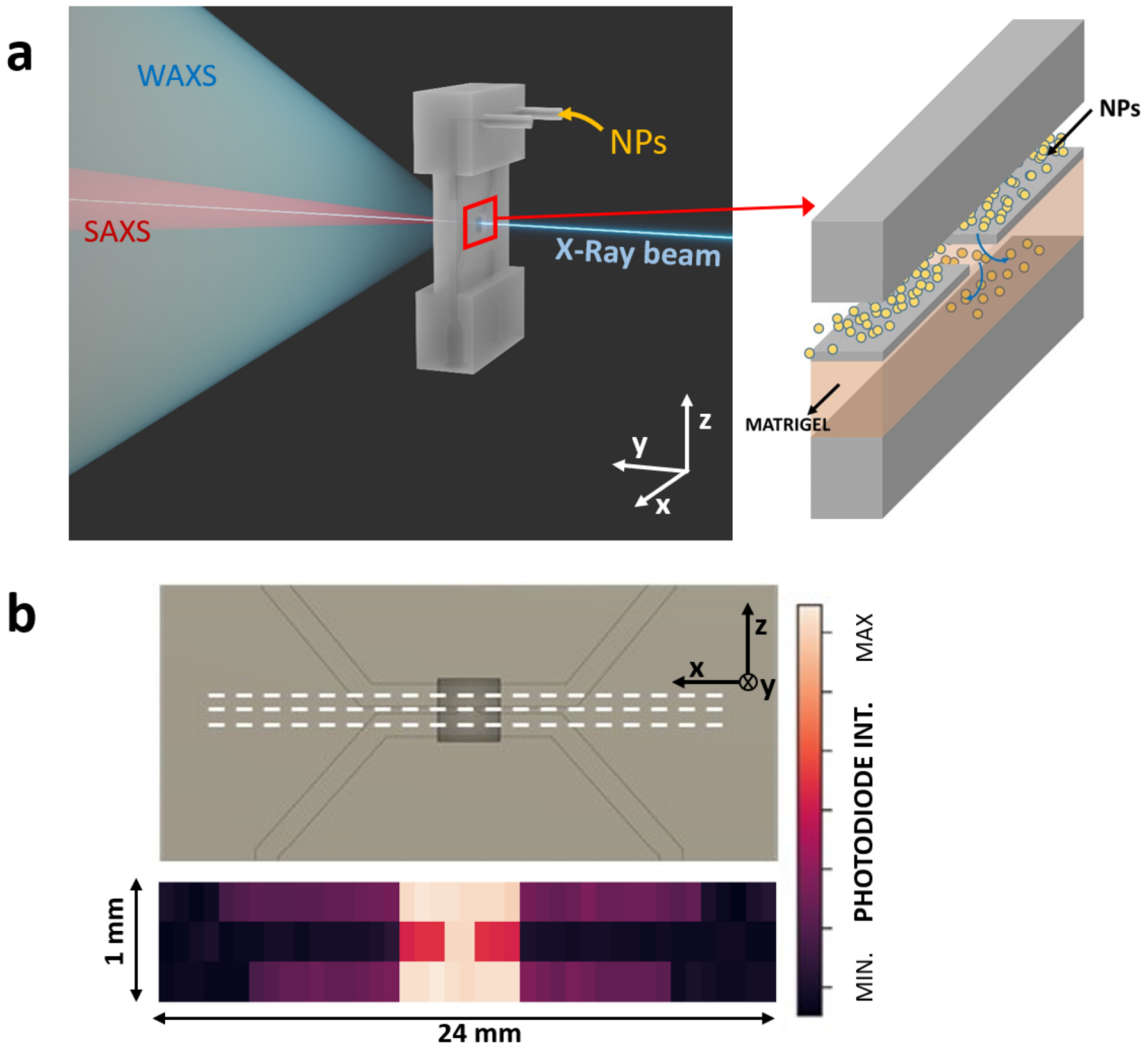

Fig. 2 **a** Experimental setup used at the NCD-SWEET BL11 beamline of the ALBA synchrotron and schematic of the arrangement of the channels relative to the incident X-ray beam. **b** X-ray transmittance map of the empty chip, obtained by plotting the normalized photodiode current, used for the alignment of the ROI of the microfluidic device. Axes were included to ease scan direction identification with respect the X-ray beam (Y axis)

The chip was vertically mounted in such a way that the NPs channel was on top, and so, the monitored NPs diffused downwards to the Matrigel channel. The microfluidic devices were filled with Matrigel (Corning, ref: 354324) at the stock concentration (10.2 mg/ml), or diluted to a concentration of 6.0 mg/ml using Dulbecco's Modified Eagle Medium Low Glucose (DMEM, Biowest ref: L0060). Both the ECM channel and corresponding reservoirs were filled with Matrigel. The device was then incubated at 37 °C for 30 min to allow the Matrigel matrix to become a gel.

To conduct the real-time diffusion measurements, precise alignment of the chip's observation window, the Region of Interest (ROI) where the nanoparticles permeate through the aperture, was meticulously carried out to coincide with the path of the X-ray beam. The ROI was identified through 2D intensity maps created using the absorption values of the empty chip. A beam size of *ca.* 40×100 μm^2 (vertical x horizontal dimensions) allowed to perform 2D mesh scans with 100 μm steps. Spatial resolution can be further improved by using smaller beams, such as those available at nano/microfocus beamlines. However, in these cases extreme caution is required to prevent matrix changes from sample heating or radiation damage due to the high beam intensity achieved. The variations in absorption values, caused by the different chip thickness at various positions, allowed to create a 2D absorption map after normalizing the photodiode current. The absorption map is shown in Fig. 2b (bottom). After the microfluidic device's alignment, the Au NPs

dispersion in water (6 nMol) was injected into the corresponding channel with a micropipette using the plugins designed as inlets, taking this as the initial experimental time. The experiments were then performed in static conditions.

Preliminary characterization of gold NPs in borosilicate glass capillaries provided both SAXS and WAXS characteristic scattering patterns. 1D scattering intensity profiles, as a function of the scattering vector ($q = 4\pi \cdot \sin\theta/\lambda$), were obtained by radial integration of the 2D patterns recorded by a Dectris Pilatus 1 M 3S (SAXS) and a Rayonix LX255-HS (WAXS) detectors, respectively, by using data reduction routines implemented at the BL11 beamline site. The SAXS curve of the raw NPs dispersion (blue line Fig. 3a) displays the typical profile of a colloidal dispersion of spherical nanoparticles [27]. The scattering curve was best fitted to a sphere model with lognormal size distribution using the SASfit software package [44, 45], resulting in a nanoparticle diameter of *ca.* 22 nm. This result is in good agreement with the 22.1 ± 2.9 nm measured by TEM (JEM-1400 Flash 120 keV, Jeol) as can be confirmed in the bottom-left inset in Fig. 3a. WAXS profile (top-right inset in Fig. 3a) allowed confirming the crystalline nature of the Au NPs.

The diffusion of nanoparticles into the Matrigel matrix was initially assessed by performing vertical scans along the interphase between the two channels. The penetration of NPs can be inferred from changes in the X-ray diffractogram. Figure 3a shows the SAXS patterns recorded at a point in the Matrigel channel, far away from the interface with the NPs channel, at the beginning of the experiment (green curve) where no NPs were present, and the SAXS pattern obtained at a point located 150 microns approximately below the interface after a time of 25 min (orange curve). As it can be observed, at this location, the profile of the SAXS pattern becomes dominated by that characteristic of the Au NPs confirming, on the one hand, their ability to penetrate the interface, and on the other hand, the ability of the NP coating to prevent their aggregation. Agglomeration of NPs would induce changes in the X-ray diffractogram, such as broadening or shifting of the characteristic scattering peaks, which are not observed [46].

The scattering profile shows a characteristic peak centered at $q = 0.55$ nm^{-1}. The area under the curve (AUC), being proportional to the number of scatters (quantity of NPs), was calculated and used to plot the NPs distribution maps. Data processing was accomplished using a custom-made Python script (Spyder IDE v. 5.4.3). To simplify the analysis, the background was subtracted from the NPs' characteristic peak as follows: $log_{10}I(background) = m \cdot log_{10}(q) + a$, where m is the slope of a line in the log–log plot and a its intercept. This approach allows avoiding the use of different backgrounds for the different regions scanned, including those with spurious reflections resulting from the X-ray beam impinging on channels walls. Afterwards, the area below the curve was calculated and used to plot the maps, which were finally normalized to their maximum value. Figure 3b shows the NPs distribution maps obtained by scanning a 1×1 mm^2 area centered in the ROI of the microfluidic device. As mentioned before, X-ray patterns were recorded every 100 μm both, in horizontal and vertical directions, providing a virtual pixel size of 100×100 μm^2 in the 2D maps presented. Higher resolution could have been achieved by using smaller step size. Nevertheless, the relatively large step employed during the scans was intended to reduce the X-ray exposure and, so, changes in the matrix due to radiation damage. The 2D scans that were recorded after a diffusion time of two hours, along with the low exposure time employed (30 s), allowed us to prevent any possible radiation damage to the matrix. Depending on the nature of the studied system, time-resolved imaging could be further improved by optimizing the exposure time or using fly-scan type measurements [47]. Compared to the step-scan method employed in this work, during fly-scan measurements the sample moves smoothly while the detector captures scattering patterns in real-time, avoiding stopping the sample stage or detector at each measurement point. Two Matrigel concentrations (6.0 and 10.2 mg/ml) were tested, showing clear differences regarding the NPs permeability, as can be appreciated in the maps. The map corresponding to the NPs diffusion throughout the high-concentration Matrigel (left) shows a limited penetration, with the NPs concentrated near the channels interface, *ca.* 200 μm far from the aperture. On the other hand, the diffusion of NPs through the low-concentration Matrigel is favoured, with NPs reaching locations hundreds of micrometres away from the channels interface. In the latter case, a certain preferential direction can be detected, suggesting that some kind of convection flow occurred, probably due to hydrostatic pressure variations arising from the differences in height between the NPs channel and the ECM channel. Considering the hydrodynamic diameter of the Au NPs, 57 ± 26 nm, according to dynamic light scattering measurements performed in a 1 nM solution (Zetasizer Nano ZS, Malvern Instruments), this difference in penetration length can be tentatively explained based on the different pore size of the Matrigel matrix, controlled by the initial Matrigel concentration used before gelation. The pore size of raw Matrigel has been estimated before to be *ca.* 140–350 nm [48]. Under these conditions, interactions between the NPs and the matrix, either through direct collision with fibres or electrostatic or hydrodynamic interactions can be anticipated, hindering the NPs

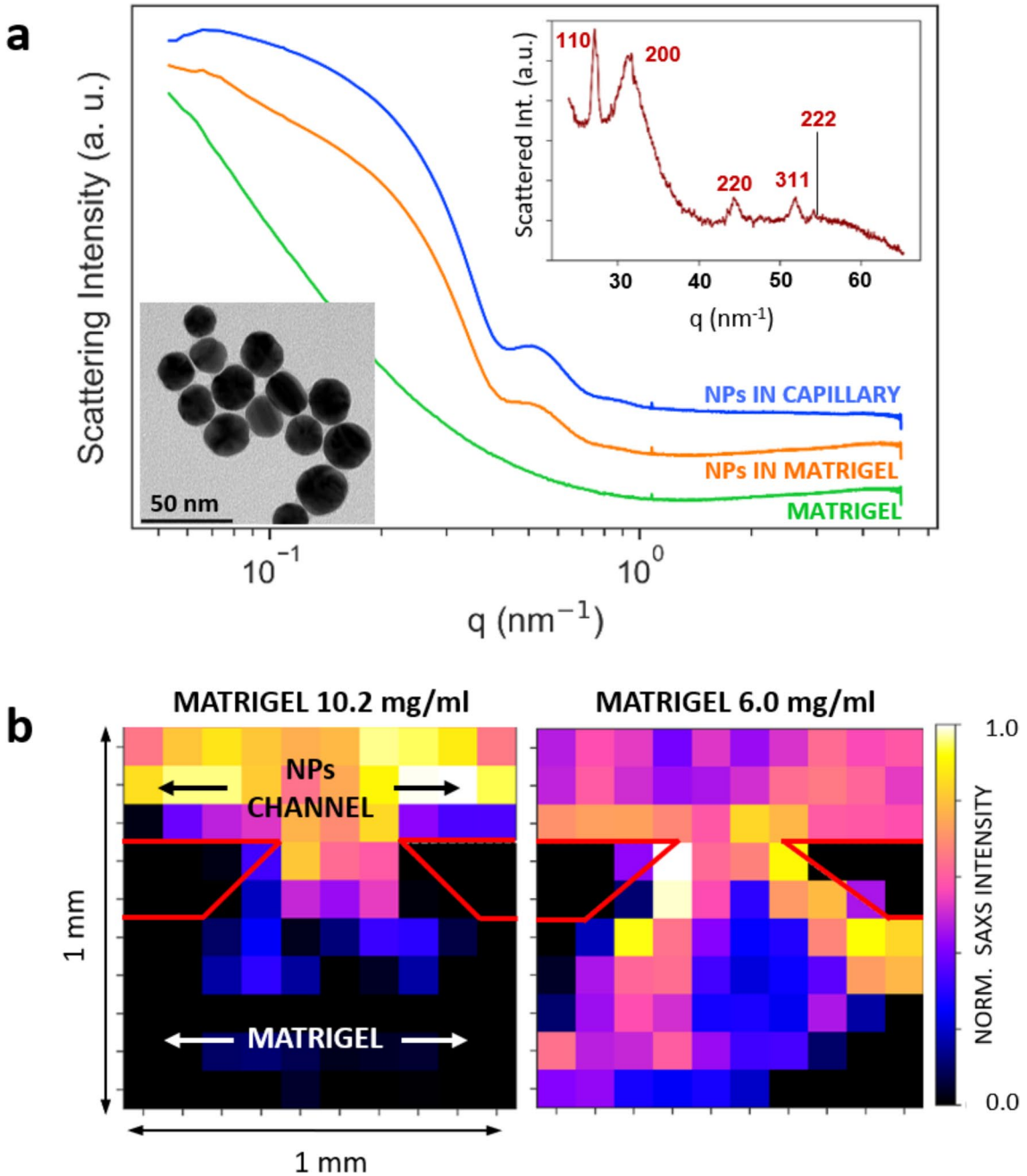

Fig. 3 **a** SAXS scattering curves corresponding to the Au NPs dispersion measured in borosilicate glass capillary (blue), Matrigel channel with no nanoparticles present (green), and in another position after the diffusion of the nanoparticles (orange). Insets show a TEM image of the Au nanoparticles and the 1D WAXS diagram including the Miller indices of the main Bragg peaks of the Au. **b** Normalized NPs concentration map diffusing into Matrigel at a concentration of 10.2 mg/ml (left) and 6 mg/ml (right). Nanoparticles and Matrigel channels are indicated with red lines revealing the channels´ separation aperture with a trapezoidal shape

diffusion [49, 50]. On the contrary, in the case of diluted Matrigel, the gel matrix pore size is expected to be larger, and as a result, the number of interactions of the NPs with the matrix is expected to be reduced, thereby favouring their diffusion. As an indirect confirmation, the beam intensity measured by the beam-stop photodiode was higher for the more porous matrix, providing direct evidence of the differing porosities. These results are in good agreement with those previously reported [51].

Conclusions

The results presented here demonstrate that the integration of microfluidics with X-ray scattering techniques using synchrotron radiation holds great promise for advancing our understanding of diffusion processes of nanomedicines within tumour-on-a-chip devices.

The approach overcomes the limitations of incorporating fluorescent labels, which can alter the interaction of NPs with biological matrix and so their diffusive properties. Microfluidic chips fabricated by stereolithography 3D printing offer significant design flexibility, while synchrotron radiation allows real-time mapping of the diffusive transport of NPs in recreated tumour microenvironments with high spatial resolution. It can be predicted that, in the future, equivalent measurements will be performed using smaller X-ray beams at nano/microfocus beamlines, in combination with more complex microfluidic devices that could be fabricated with higher resolution.

The present study specifically reveals the impact of matrix porosity on the diffusive transport of oligonucleotide functionalized gold NPs and holds a great potential to perform studies regarding other factors influencing NP's diffusion processes depending both, on the nature of the nanomedicine (size, shape, concentration) or the matrix (temperature, pH, composition, etc.). Further work will allow for the identification of nanomedicine key transport parameters in complex biological matrices, such as diffusion coefficients, effective diffusion length or effective diffusion time.

Acknowledgements

This work has been partially performed under the framework of the EVONANO project funded by the European Union's Horizon 2020 FET-Open program under grant agreement No. 800983. It was supported by the Spanish Ministry of Economy and Competitiveness [PID2020-119352RB-I00], Comunidad de Madrid [S2022/BMD-7403 RENIM-CM], Asociación Española Contra el Cáncer, and IMDEA Nanociencia. A.M.A. acknowledges a predoctoral scholarship from the Spanish Ministry of Science and Innovation Severo Ochoa Program for Centers of Excellence in R&D (Grant No: PRE2019-88686). I.P. acknowledges a predoctoral grant from the Community of Madrid for the hiring of predoctoral research staff for the year 2022 (Grant No: PIPF-2022SAL-GL-24788). IMDEA Nanoscience receives support from the 'Severo Ochoa' Programme for Centres of Excellence in R&D (MICINN Grant no: CEX2020-001039-S). Experiments were performed at the NCD-SWEET BL11 beamline at ALBA Synchrotron with the collaboration of the ALBA staff.

Author contributions

A.M.A: Conceptualization, formal analysis, investigation, methodology, software, validation, visualization, writing (original draft) and supervision. I.P: Investigation, writing (review and editing). R.M.: Investigation. D.P.: Investigation. J.P.F-B: Investigation, resources, writing (review and editing). J.C.M-G: Methodology, software, resources, writing (review and editing). M.C.: Conceptualization, writing (review and editing). J.J.H.: Conceptualization, formal analysis, investigation, methodology, validation, visualization, writing (review and editing), supervision and funding acquisition. Á.S.: Writing (review and editing), resources, funding acquisition. I.R.: Conceptualization, supervision, resources, project administration, writing (review and editing), funding acquisition.

Availability of data and materials

The datasets generated and/or analysed during the current study are available in the IMDEA Nanociencia repository following the next link: https://hdl.handle.net/20.500.12614/3809.

Declarations

Competing interests

The authors declare no competing interests.

Received: 7 August 2024 Accepted: 22 October 2024
Published online: 02 November 2024

References

1. Sung H, Ferlay J, Siegel RL, Laversanne M, Soerjomataram I, Jemal A, Bray F (2021) Global cancer statistics 2020: GLOBOCAN estimates of incidence and mortality worldwide for 36 cancers in 185 countries. CA Cancer J Clin 71(3):209–249
2. Portillo-Lara R, Annabi N (2016) Microengineered cancer-on-a-chip platforms to study the metastatic microenvironment. Lab Chip 16(21):4063–4081
3. Morales-Espinosa D, García-Román S, Teixidó C, Karachaliou N, Rosell R (2015) Immunotherapy meets targeted therapy: will this team end the war against cancer? Transl Lung Cancer Res 4(6):752–755
4. Atkins MB, Larkin J (2016) Immunotherapy combined or sequenced with targeted therapy in the treatment of solid tumors: current perspectives. J Natl Cancer Inst 108(6):1–9
5. Seleci M, Ag Seleci D, Joncyzk R, Stahl F, Blume C, Scheper T (2016) Smart multifunctional nanoparticles in nanomedicine. BioNanoMaterials 17(1–2):33–41
6. Peer D, Karp JM, Hong S, Farokhzad OC, Margalit R, Langer R (2007) Nanocarriers as an emerging platform for cancer therapy. Nat Nanotechnol 2:751–760
7. Hua S, de Matos MBC, Metselaar JM, Storm G (2018) Current trends and challenges in the clinical translation of nanoparticulate nanomedicines: pathways for translational development and commercialization. Front Pharmacol 9:1–14
8. Llop J, Lammers T (2021) Nanoparticles for cancer diagnosis, radionuclide therapy and theranostics. ACS Nano 15(11):16974–16981
9. Wilhelm S, Tavares AJ, Dai Q, Ohta S, Audet J, Dvorak HF, Chan WCW (2016) Analysis of nanoparticle delivery to tumours. Nat Rev Mater 1(5):16014
10. Jain RK, Stylianopoulos T (2010) Delivering nanomedicine to solid tumors. Nat Rev Clin Oncol 7(11):653–664
11. Salvioni L, Rizzuto MA, Bertolini JA, Pandolfi L, Colombo M, Prosperi D (2019) Thirty years of cancer nanomedicine: success, frustration, and hope. Cancers 11(12):1855
12. Trujillo-de Santiago G, Flores-Garza BG, Tavares-Negrete JA, Lara-Mayorga IM, González-Gamboa I, Zhang YS, Rojas-Martínez A, Ortiz-López R, Álvarez MM (2019) The tumor-on-chip: recent advances in the development of microfluidic systems to recapitulate the physiology of solid tumors. Materials 12(18):2945
13. Wan L, Neumann CA, Leduc PR (2020) Tumor-on-a-chip for integrating a 3D tumor microenvironment: chemical and mechanical factors. Lab Chip 20(5):873–888
14. Albanese A, Lam AK, Sykes EA, Rocheleau JV, Chan WCW (2013) Tumour-on-a-chip provides an optical window into nanoparticle tissue transport. Nat Commun 4(1):2718
15. Carvalho V, Bañobre-López M, Minas G, Teixeira SFCF, Lima R, Rodrigues RO (2022) The integration of spheroids and organoids into organ-on-a-chip platforms for tumour research: a review. Bioprinting 27(June):e00224
16. Wang Y, Cuzzucoli F, Escobar A, Lu S, Liang L, Wang S (2018) Tumor-on-a-chip platforms for assessing nanoparticle-based cancer therapy. Nanotechnology 29(33):332001

17. Shah PN, Lin TY, Aanei IL, Klass SH, Smith BR, Shaqfeh ESG (2018) Extravasation of Brownian Spheroidal Nanoparticles through Vascular Pores. Biophysj 115(6):1103–1115
18. Dávila S, Cacheux J, Rodríguez I (2021) Microvessel-on-chip fabrication for the in vitro modeling of nanomedicine transport. ACS Omega 6(39):25109–25115
19. Martín-Asensio A, Dávila S, Cacheux J, Lindstaedt A, Dziadosz A, Witt D, Calero M, Balaz I, Rodríguez I (2023) Recapitulating solid stress on tumor on a chip for nanomedicine diffusive transport prediction. Adv NanoBiomed Res 3(6):1–12
20. Huang K, Boerhan R, Liu C, Jiang G (2017) Nanoparticles penetrate into the multicellular spheroid-on-chip: effect of surface charge, protein corona, and exterior flow. Mol Pharm 14(12):4618–4627
21. Wang HF, Ran R, Liu Y, Hui Y, Zeng B, Chen D, Weitz DA, Zhao CX (2018) Tumor-vasculature-on-a-chip for investigating nanoparticle extravasation and tumor accumulation. ACS Nano 12(11):11600–11609
22. Ho YT, Adriani G, Beyer S, Nhan PT, Kamm RD, Kah JCY (2017) A facile method to probe the vascular permeability of nanoparticles in nanomedicine applications. Sci Rep 7(1):1–13
23. Barbato MG, Pereira RC, Mollica H, Palange A, Ferreira M, Decuzzi P (2021) A permeable on-chip microvasculature for assessing the transport of macromolecules and polymeric nanoconstructs. J Colloid Interface Sci 594:409–423
24. Zhang L, Gu FX, Chan JM, Wang AZ, Langer RS, Farokhzad OC (2008) Nanoparticles in medicine: therapeutic applications and developments. Clin Pharmacol Ther 83(5):761–769
25. Davis ME, Chen Z, Shin DM (2008) Nanoparticle therapeutics: an emerging treatment modality for cancer. Nat Rev Drug Discov 7(9):771–782
26. Guo X, Gutsche A, Wagner M, Seipenbusch M, Nirschl H (2013) Simultaneous SWAXS study of metallic and oxide nanostructured particles. J Nanoparticle Res. https://doi.org/10.1007/s11051-013-1559-8
27. Li T, Senesi AJ, Lee B (2016) Small angle X-ray scattering for nanoparticle research. Chem Rev 116(18):11128–11180
28. Chu B, Liu T (2000) Characterization of nanoparticles by scattering techniques. J Nanoparticle Res 2(1):29–41
29. Coral DF, Soto PA, de Sousa E, Brollo MEF, Mera-Córdoba JA, Mendoza Zélis P, Setton-Avruj CP, Roig A, Fernández van Raap MB (2022) Small-angle X-ray scattering to quantify the incorporation and analyze the disposition of magnetic nanoparticles inside cells. J Colloid Interface Sci 608(September 2021):1–12
30. Modena MM, Rühle B, Burg TP, Wuttke S (2019) Nanoparticle characterization: what to measure? Adv Mater 31(32):1–26
31. Le Goas M, Testard F, Taché O, Debou N, Cambien B, Carrot G, Renault JP (2020) How do surface properties of nanoparticles influence their diffusion in the extracellular matrix? A model study in matrigel using polymer-grafted nanoparticles. Langmuir 36(35):10460–10470
32. Ilhan-Ayisigi E, Yaldiz B, Bor G, Yaghmur A, Yesil-Celiktas O (2021) Advances in microfluidic synthesis and coupling with synchrotron SAXS for continuous production and real-time structural characterization of nano-self-assemblies. Colloids Surfaces B Biointerfaces 201(2020):111633
33. Gimondi S, Ferreira H, Reis RL, Neves NM (2023) Microfluidic devices: a tool for nanoparticle synthesis and performance evaluation. ACS Nano 17(15):14205–14228
34. Seibt S, Ryan T. Microfluidics for time-resolved small-angle X-ray scattering. In Adv. Microfluid. Nanofluids, (IntechOpen, 2021), 13.
35. Bai X, Wang J, Mu Q, Su G (2021) In vivo protein corona formation: characterizations, effects on engineered nanoparticles' biobehaviors, and applications. Front Bioeng Biotechnol 9(March):1–16
36. Huang CP, Lu J, Seon H, Lee AP, Flanagan LA, Kim H-Y, Putnam AJ, Jeon NL (2009) Engineering microscale cellular niches for three-dimensional multicellular co-cultures. Lab Chip 9(12):1740
37. Ghazal A, Lafleur JP, Mortensen K, Kutter JP, Arleth L, Jensen GV (2016) Recent advances in X-ray compatible microfluidics for applications in soft materials and life sciences. Lab Chip 16(22):4263–4295
38. J.I. Cutler, E. Auyeung, and C.A. Mirkin (2021) Spherical Nucleic Acids Vol. 1 1, 91–136
39. Rois PM, Latorre A, Diaz CR, del Moral Á, Somoza Á (2018) Reprogramming cells for synergistic combination therapy with nanotherapeutics against uveal melanoma. Biomimetics 3(4):28
40. Liu S, Yu CY, Wei H (2023) Spherical nucleic acids-based nanoplatforms for tumor precision medicine and immunotherapy. Mater Today Bio 22(May):100750
41. Prigodich AE, Randeria PS, Briley WE, Kim NJ, Daniel WL, Giljohann DA, Mirkin CA (2012) Multiplexed nanoflares: MRNA detection in live cells. Anal Chem 84(4):2062–2066
42. Latorre A, Posch C, Garcimartan Y, Ortiz-Urda S, Somoza A (2014) Single-point mutation detection in RNA extracts using gold nanoparticles modified with hydrophobic molecular beacon-like structures. Chem Commun 50(23):3018–3020
43. Turkevich J, Stevenson PC, Hillier J (1951) A study of the nucleation and growth processes in the synthesis of colloidal gold. Discuss Faraday Soc 11(1):55
44. Breßler I, Kohlbrecher J, Thünemann AF (2015) SASfit : a tool for small-angle scattering data analysis using a library of analytical expressions. J Appl Crystallogr 48(5):1587–1598
45. Kohlbrecher J, Breßler I (2022) Updates in SASfit for fitting analytical expressions and numerical models to small-angle scattering patterns. J Appl Crystallogr 55(6):1677–1688
46. Appel C, Kuttich B, Kraus T, Stühn B (2021) In situ investigation of temperature induced agglomeration in non-polar magnetic nanoparticle dispersions by small angle X-ray scattering. Nanoscale 13:6916–6920
47. Yang L, Liu J, Chodankar S, Antonelli S, DiFabio J (2022) Scanning structural mapping at the life science X-ray scattering beamline. J Synchrotron Rad 29:540–54849
48. Tomasetti L, Liebl R, Wastl DS, Breunig M (2016) Influence of PEGylation on nanoparticle mobility in different models of the extracellular matrix. Eur J Pharm Biopharm 108:145–155
49. Engin AB, Nikitovic D, Neagu M, Henrich-Noack P, Docea AO, Shtilman MI, Golokhvast K, Tsatsakis AM (2017) Mechanistic understanding of nanoparticles' interactions with extracellular matrix: the cell and immune system. Part Fibre Toxicol 14(1):1–16
50. Barua S, Mitragotri S (2014) Challenges associated with penetration of nanoparticles across cell and tissue barriers: a review of current status and future prospects. Nano Today 9(2):223–243
51. He X, Yang Y, Han Y, Cao C, Zhang Z, Li L, Xiao C, Guo H, Wang L, Han L, Qu Z, Liu N, Han S, Xu F (2023) Extracellular matrix physical properties govern the diffusion of nanoparticles in tumor microenvironment. Proc Natl Acad Sci 120(1):2017

Publisher's Note